Sustainable Energy & Fuels

ROYAL SOCIETY OF CHEMISTRY

PAPER

View Article Online
View Journal | View Issue

Open Access Article. Published on 15 November 2021. Downloaded on 2/12/2026 8:14:27 AM.
This article is licensed under a Creative Commons Attribution-NonCommercial 3.0 Unported Licence.

Check for updates

Cite this: *Sustainable Energy Fuels*, 2021, **5**, 6498

Shelf lifetime analysis of organic solar cells combining frequency and time resolved techniques†

Alfonsina Abat Amelenan Torimtubun, *[a] Maria Méndez, [b] José G. Sánchez, [b] Josep Pallarès, *[a] Emilio Palomares *[bc] and Lluis F. Marsal *[a]

Received 20th July 2021
Accepted 3rd November 2021

DOI: 10.1039/d1se01107c

rsc.li/sustainable-energy

The device operational lifetime and the understanding of the degradation pathways are critical steps for inverted organic solar cells (iOSCs) to enter the energy market. In this work, a combined study of impedance spectroscopy (IS) and photovoltage/photocurrent transient (TPV/TPC) techniques was employed to analyze the degradation of PTB7-Th:$PC_{70}BM$-based iOSCs in accordance with the ISOS-D1 protocol under ambient conditions without encapsulation. Both techniques provide real information on how devices with different electron transport layers (PFN, TiO_x, and ZnO) were degraded, affecting the stability of the active layer. We found that the main cause of degradation is the formation of interface traps in the dark and upon air exposure. The increase of trap density in the active layer upon degradation was revealed by TPV. The change in interface trap density due to the interfacial defect over the shelf-lifetime was further confirmed by the data from IS measurements. Last but not least, modelling dark current–voltage (*J*–*V*) using the IS data as well as the morphological changes of each ETL verified our hypothesis.

Introduction

Emerging photovoltaic technologies such as dye sensitized solar cells, perovskite solar cells, and organic solar cells have established their significance as sustainable solar to energy devices. Organic solar cells (OSCs), in contrast to current perovskite solar cells, are lead-free and low-cost with a short energy payback time, and can be solution processed on light-weight, semitransparent, flexible substrates over large areas by the roll-to-roll technique.[1–5] Along with these appealing properties, in recent years, a rapid improvement in power conversion efficiency (PCE) up to over 18% in single-junction OSCs may endow OSCs with an opportunity to enter the market.[6–8] However, high efficiency and low cost are not the only requirements to scale up OSC devices in the market. Device operational stability is also one of the key criteria to make the large-scale production of OSCs commercially more feasible. Up to now, silicon-based photovoltaic (PV) companies guarantee their products for 25 years of operational stability.[9] For OSCs, a lifetime of over 20 years is estimated to be financially competitive,[10] giving space for further device stability improvement.

A huge effort is being made to understand the degradation mechanisms and strategies to make the OSC lifetime longer. For instance, modifying the chemical structure of the active layer materials, employing a ternary strategy for the active layer, using a compatibilizer to reduce the interfacial tension, inverting the OSC device polarity, optimizing buffer layers, using stable electrodes, eliminating the photo-dimerization of fullerenes, and increasing the material crystallinity of non-fullerene materials are known degradation mechanisms to minimize the intrinsic degradation.[11–15] Meanwhile, a proper encapsulation is widely used to prevent the interaction of oxygen and moisture from the atmosphere with OSC devices. This method can lead to the suppression of the device extrinsic degradation. Nevertheless, the production cost, weight, and device flexibility are important concerns from the industrial engineering perspective when the devices need to be encapsulated. It is hence highly desirable to improve the intrinsic stability and minimize the encapsulation.

Some studies on polymer:fullerene OSCs showed that the inverted structure and the choice of the metal oxide, stable metal or electron transport polymer for the cathode material have a key contribution to improve the air stability of the device.[16–18] In iOSCs, the use of hygroscopic and acidic poly(3,4-ethylenedioxythiophene):poly(styrene sulfonic acid) (PEDOT:PSS) can be avoided and the low work function

[a]*Department of Electric, Electronic and Automatic Engineering, Universitat Rovira I Virgili, 43007 Tarragona, Spain. E-mail: josep.pallares@urv.cat; lluis.marsal@urv.cat*
[b]*Institute of Chemical Research of Catalonia (ICIQ-BIST), 43007 Tarragona, Spain. E-mail: epalomares@iciq.es*
[c]*Catalan Institution for Research and Advanced Studies (ICREA), 08010 Barcelona, Spain*

† Electronic supplementary information (ESI) available: Experimental section, dark *J*–*V* fitting, modelled normalized PCE, AFM, CE and DC techniques, J_{SC} and V_{OC} *vs.* light intensity, capacitance & resistance values and IS data. See DOI: 10.1039/d1se01107c

 This journal is © The Royal Society of Chemistry 2021

Open Access Article. Published on 15 November 2021. Downloaded on 2/12/2026 8:14:27 AM.
This article is licensed under a Creative Commons Attribution-NonCommercial 3.0 Unported Licence.

aluminium electrode that causes the degradation can be replaced with a high work function metal electrode such as silver or gold.[19] The electron transport layer (ETL) is a key component in acquiring high performance and stable iOSCs. The ETL has a role in modifying the alignment between the work function of the transparent conductive ITO cathode and the Fermi level of the semiconductor, promoting the electron transfer and the carrier extraction process.[20,21] To improve the stability, the ETL may act as a scavenging layer to protect the active layer from oxygen and moisture.[17] Transition metal oxides as ETLs, such as titanium dioxide (TiO_x) and zinc oxide (ZnO), and water-soluble organic ETLs, poly[(9,9-bis(3′-(*N*,*N*-dimethylamino)propyl)-2,7-fluorene)-*alt*-2,7-(9,9-dioctyl-fluorene)] (PFN), are the most common ETLs used in iOSCs. These ETL materials exhibit high electron conductivity, an excellent optical transmittance, a low work function, a high refractive index, good chemical stability, non-toxicity, and an ability to improve charge carrier extraction.[22–25]

It is apparent that interlayer engineering and its optimization are the crucial factors to be considered to fabricate high performance and air-stable devices. To gain further insight into the physical mechanisms governing the device operation, optoelectronic characterization techniques are widely employed. Small-perturbation time- and frequency-domain measurements such as transient photovoltage/photocurrent (TPV/TPC) spectroscopy, charge extraction, and impedance spectroscopy (IS) have been widely employed to study relaxation processes in the field of dye-sensitized solar cells (DSSCs),[26,27] OSCs,[28,29] and perovskite solar cells,[30] but fewer studies focused on the combination of both techniques. Electronic transitions can be studied with TPV/TPC on a very fast time scale (higher frequency), while the electronic and ionic conduction can be observed by IS on lower time scales (lower frequency).[31] Nevertheless, the same information and comparable results can be obtained from TPV/TPC or EIS. Combined TPV and IS techniques have already been used by Pockett *et al.* to study the effect of degradation on the active layer and interlayer in OSCs.[32] However, in-depth discussion of device lifetime analysis according to ISOS protocols using combined TPV and IS techniques remains unclear. In the meantime, ISOS protocols play an important role in the advancement of OSC's research and future industrial manufacture.

In this study, we perform IS and TPV/TPC measurements on an inverted PTB7-Th:$PC_{70}BM$-based device with different ETL materials to investigate the effect of the ETL on the stability of nonencapsulated iOSCs. The standard procedure of the ISOS D-1 protocol (under dark and ambient conditions) was used for an accurate lifetime determination.[33] Three different ETLs were investigated: one water-soluble organic-based (PFN) and two metal oxide-based (TiO_x and ZnO). We demonstrate that TPV/TPC combined with IS can be employed to gain a deeper insight into the behavior and degradation mechanisms of iOSCs concerning the cathode interlayer used. The TPV measurements are useful in observing the degradation of the active layer as a result of trap formation, while the IS measurements give more detailed information about the interfacial density of states across the interlayer. We found that using an appropriate ETL can significantly improve the stability of iOSCs. Under nonencapsulated ambient conditions, metal oxides show a more stable ETL while organic interlayers are more susceptible to oxygen and moisture ingress.

Results & discussion

Photovoltaic characteristics obtained by current–density (*J*–*V*) measurements

In this study, bulk heterojunction (BHJ) devices were fabricated with an inverted configuration ITO/ETL/PTB7-Th:$PC_{70}BM$/V_2O_5/Ag as schematically illustrated in Fig. 1a by using different ETL materials. An inverted structure is chosen to minimize any degradation originating from metal electrode oxidation and the acidic interfacial layer.[34] The selected interlayers studied here represent the most common organic and inorganic materials employed as ETLs in iOSCs. The as-fabricated device namely "fresh device" was characterized immediately after the fabrication process. The nonencapsulated fresh devices were then kept in an ambient environment (room temperature (RT) of 23–27 °C and controlled relative humidity (RH) of 35–50%) under open circuit conditions with no illumination, following the ISOS-D1 protocol.[33] The devices were only exposed to light during device characterization and returned to the dark shelf chamber.

Fig. 1b shows the current density–voltage (*J*–*V*) characteristics of these fresh and degraded cells measured under simulated AM 1.5G illumination (100 mW cm^{-2}) at RT. The corresponding device parameters are summarized in Table 1. In addition, Fig. S1a–c† show the initial transient of the illuminated *J*–*V* measurements. As for the performance of the fresh device, ZnO-iOSC shows the lowest J_{SC}, the lowest shunt resistance (R_{Sh}), and thus the lowest PCE_{max} of 9.79%. TiO_x-iOSC exhibits the highest J_{SC}, the lowest FF and the highest series resistance (R_S), resulting in a PCE_{max} of 9.99%. Meanwhile, PFN-iOSC can improve the device performance, showing the highest V_{OC}, FF and R_{Sh}, which leads to the highest PCE_{max} of 10.35%. From the degradation perspective, degraded (526 h) devices show a prominent reduction in the device performance for all ETLs compared to the fresh (0 h) devices. The J_{SC} of PFN-, TiO_x-, and ZnO-iOSCs fell 13%, 9% and 7% after 526 h. The J_{SC} reduction in all degraded cells is coherent with the reduction of calculated J_{SC} values obtained from external quantum efficiency when compared to those of fresh devices, as shown in Fig. 1c. On the other hand, V_{OC} decreases slightly after degradation, fell 10% for PFN-iOSC and fell 4% for each TiO_x- and ZnO-iOSC. In addition, a significant decrease in FF after 526 h degradation is observed; FF fell by 33%, 17% and 16% for PFN-, TiO_x- and ZnO-iOSCs, respectively. A significance FF reduction may arise from a gradual increase of R_S and a drop of R_{Sh} is observed for degraded devices as a result of the parasitic resistance effect. It leads to a considerably lower PCE, where the PCE of PFN-iOSC drops to almost 50% of its initial value while those of TiO_x- and ZnO-iOSCs drop to 26% and 24% from their initial value. In general, the devices using PFN as the cathode interlayer in iOSCs suffer from the worst stability, while the devices using ZnO as the ETL resulted in the most stable devices. Since the device architecture and fabrication process are identical, the

Open Access Article. Published on 15 November 2021. Downloaded on 2/12/2026 8:14:27 AM.
This article is licensed under a Creative Commons Attribution-NonCommercial 3.0 Unported Licence.

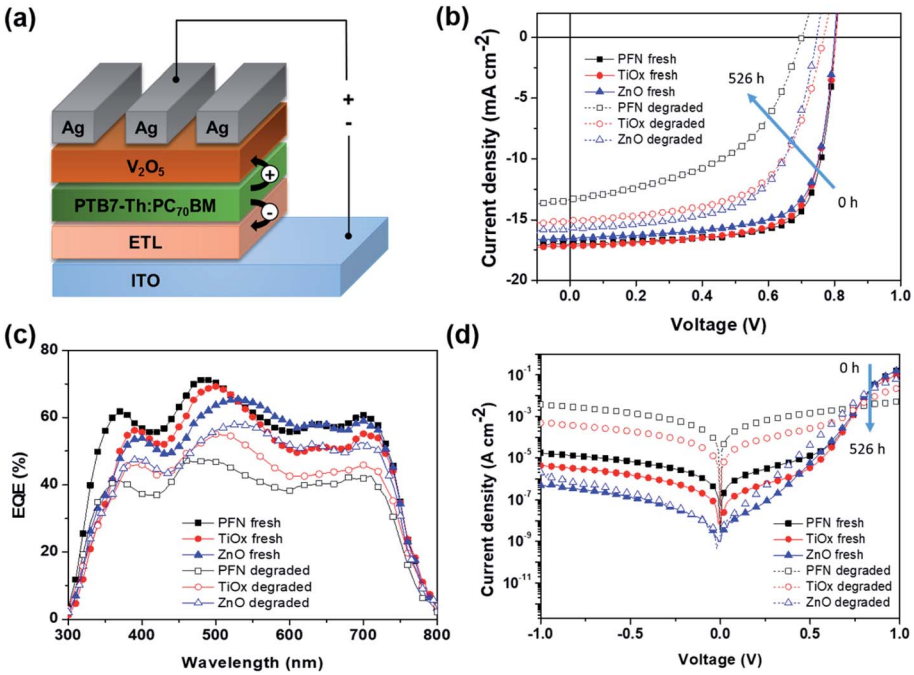

Fig. 1 (a) Schematic illustration of the inverted device architecture, (b) J–V characteristics under illumination, (c) EQE spectra, and (d) dark J–V characteristics of fresh and 526 h degraded PTB7-Th:PC_{70}BM-based devices with different ETLs (PFN, TiO_x and ZnO).

difference in device parameter stability observed may be attributed to the different ETL materials used.

Fig. 1d further compares the dark J–V characteristics of all devices before and after 526 hours of degradation. Table S1† summarizes the experimental and modeled device performance parameters from dark J–V curves. The fitting values are obtained using a two-diode equivalent model, where the detailed fitting calculation can be found elsewhere.[35] In addition, Fig. S1d–f† show the initial transient of the dark J–V measurements and Fig. S2† displays the fitting for the fresh and degraded devices. All fresh devices show an ideal exponential region with an ideality factor in the range of 1.05 to 1.11, combined with R_S at medium–high voltage bias and a leakage current at low bias, which can be linked to the manufacturing imperfections.[36] The leakage current depends on the ETL and can be ascribed to the combination of a R_{Sh} and a second non-ideal exponential region with an ideality factor larger than 2. A high leakage current is probably caused by lower contact selectivity within the cell and higher surface energy when aged in the presence of water and oxygen.[37,38] After 526 h degradation, all devices show a reduction in the current density in forward and reverse biases due to the loss in diode and resistance properties. The observed R_S increment in all degraded devices can be ascribed to several factors such as the creation of deep and shallow traps due to the interaction of oxygen and water with the polymer reducing charge carrier mobility, a loss of injection efficiency from the electrode contact into the active layer due to increasing barrier for charge injection or the creation of an isolation layer between the bulk active layer and contact hindering the charge carrier collection.[39] In addition, the ideality factor values of the degraded devices in the first exponential region change to 1.59–1.91 and the leakage current strongly increases due to the reduction of R_{Sh} values and the worsening of the second exponential region, with ideality factors much larger than 2. Therefore, the lower PCE observed in PFN-iOSC and TiO_x-iOSC than those of ZnO-iOSC could be due to lower charge extraction and higher leakage current. Therefore, the lower PCE observed in PFN-iOSC and TiO_x-iOSC than those of ZnO-iOSC could be due

Table 1 Device performance parameters of the relevant ETLs (PFN, TiO_x and ZnO), measured under AM 1.5G with 100 mW cm^{-2} intensity. Nonencapsulated devices were degraded after 526 h under ambient conditions (RT = 23–27 °C and % RH = 35–50%)

ETL		J_{SC} (J_{calc})[a] [mA cm^{-2}]	V_{OC} [V]	FF [%]	PCE (PCE_{max}) [%]	R_S [Ω cm^2]	R_{Sh} [Ω cm^2]
PFN	Fresh	16.83 ± 0.37 (15.98)	0.80 ± 0.006	74.40 ± 0.52	10.00 ± 0.20 (10.35)	0.95 ± 0.06	1618 ± 542
	Degraded	14.69 ± 0.93 (14.04)	0.71 ± 0.018	50.21 ± 1.22	5.31 ± 0.36 (5.89)	7.94 ± 1.08	242 ± 23
TiO_x	Fresh	17.19 ± 0.17 (16.71)	0.79 ± 0.005	71.40 ± 1.12	9.73 ± 0.18 (9.99)	1.69 ± 0.08	1044 ± 315
	Degraded	15.71 ± 0.39 (15.01)	0.76 ± 0.004	59.43 ± 1.62	7.11 ± 0.32 (7.39)	5.16 ± 2.04	543 ± 63
ZnO	Fresh	16.70 ± 0.20 (15.43)	0.79 ± 0.005	72.45 ± 0.61	9.60 ± 0.14 (9.79)	0.94 ± 0.07	858 ± 424
	Degraded	15.53 ± 0.32 (14.47)	0.76 ± 0.017	61.17 ± 1.86	7.21 ± 0.25 (7.41)	2.78 ± 1.27	531 ± 132

[a] The J_{calc} is the integrated current density calculated from the EQE spectra.

Open Access Article. Published on 15 November 2021. Downloaded on 2/12/2026 8:14:27 AM.
This article is licensed under a Creative Commons Attribution-NonCommercial 3.0 Unported Licence.

to lower charge extraction and higher leakage current, which are limiting factors that correlated with the higher trap defects upon degradation, as described later in this work.

To get a further insight into the degradation trend behavior of iOSCs with different ETLs over shelf lifetime in an ambient environment, the normalized device performance parameters (V_{OC}, J_{SC}, FF and PCE) are presented in Fig. 2. Corresponding to the ISOS-D1 protocol, the operating shelf lifetime of each studied cell is summarized in Table 2. The term E_0 is the initial testing measurement of fresh devices at 0 h (T_0), while E_{80} is the testing measurement of degraded devices under dark ambient conditions after the PCE decays 20% from its initial value at time T_{80}.[33] Fig. 2a shows the PCE decay behavior of all devices. It is worth noting that rapid PCE decay in the first few hours is observed in all devices. It is known as the "burn-in loss" degradation loss mechanism due to the photochemical reaction within the device layers.[40,41] It can be seen that PFN-iOSC degraded to 80% of its initial PCE (T_{80}) after only 26 h, faster than its TiO_x- and ZnO-iOSC counterparts that took 341 h (2 weeks) and 526 h (3 weeks) to reach T_{80}, suggesting the poor stability of PFN as the ETL in nonencapsulated iOSCs. It is because their performance parameter decreases rapidly in a short exposure time, as shown in Fig. 2b and Table 2. The V_{OC}, J_{SC}, and FF of PFN-iOSC at T_{80} are reduced down to 4%, 6% and 16%, while those of TiO_x-iOSC at T_{80} fall to 3%, 7%, and 11% (Fig. 2c) and those of ZnO-iOSC at T_{80} are decreased down to 5%, 8%, and 14% (Fig. 2d), respectively. The evolution of illuminated and dark J–V characteristics over the device lifetimes is shown in Fig. S1.† In general, compared to the other device parameters, V_{OC} seems to be the least affected by the degradation in PTB7-Th:$PC_{70}BM$-based iOSCs, while J_{SC} and FF appear to suffer more by the degradation. It suggests that the performance deterioration is probably more associated with the charge extraction and leakage current-dominated photogeneration, which is correlated with the interlayer quality of the devices.

Table 2 The summary of shelf lifetime data for all the nonencapsulated devices under ambient conditions (RT, % RH = 35–50%). The data given are in hours

Standard lifetime	PFN	TiO_x	ZnO
E_0, T_0 (PCE, %)	10.35	9.99	9.79
T_{95}	3	8	7
T_{90}	9	70	115
T_{85}	12	224	224
T_{80}	26	341	526

As displayed in Fig. 2a, the degradation of all devices displays an exponential decay. A fast initial decay followed by a slow decay can be fitted by the superposition of two exponential functions with different time constants, as previously reported:[18,42]

$$\frac{\mathrm{PCE}(t)}{\mathrm{PCE}(0)} = A1 \times \exp\left(\frac{-t}{T1}\right) + A2 \times \exp\left(\frac{-t}{T2}\right) \quad (1)$$

where PCE(0) is the relative initial power conversion efficiency at $t = 0$ h. The time constants ($T1$ and $T2$) and the degradation power factors of the individual exponential functions ($A1$ and $A2$) are obtained *via* a least-squares fit. The two exponential functions of the measured and modeled curves for each ETL using

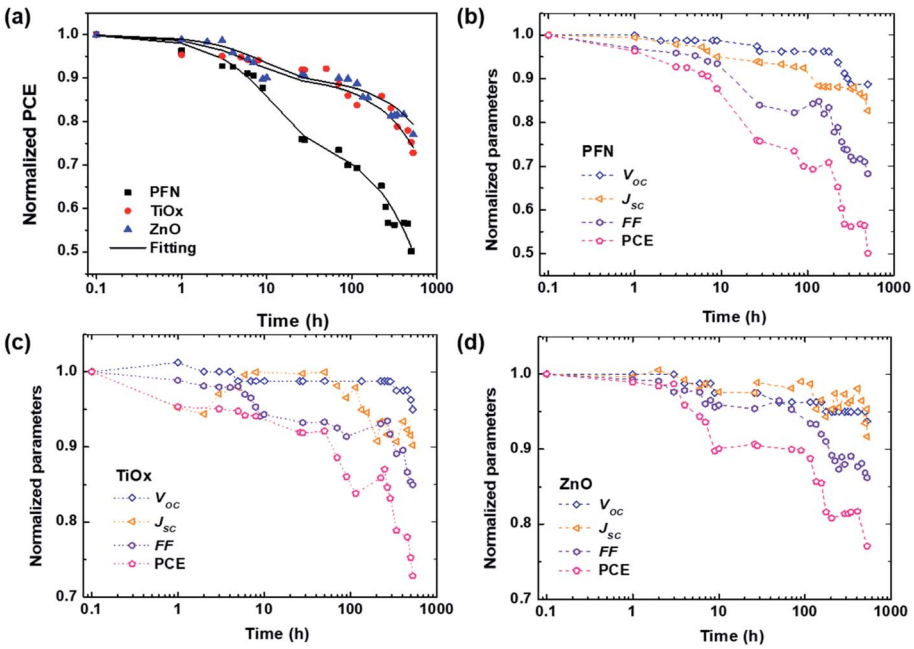

Fig. 2 (a) Fitting of the normalized PCE over the storage time using eqn (1) for all devices. (b)–(d) Normalized device performance parameters of each inverted PTB7-Th:$PC_{70}BM$-based device with different ETLs: (b) PFN, (c) TiO_x, and (d) ZnO. The symbols are the experimental data, the solid lines are the fitting curves, and the dashed lines are guide to the eyes. The samples were degraded in dark ambient environment and all measurements were carried out under AM 1.5G illumination.

Open Access Article. Published on 15 November 2021. Downloaded on 2/12/2026 8:14:27 AM.
This article is licensed under a Creative Commons Attribution-NonCommercial 3.0 Unported Licence.

equation 1 can be observed clearly in Fig. S3 and Table S2† summarizes the values extracted from eqn (1) for all devices. It is observed that metal oxide ETL-based devices (ZnO-iOSC and TiO_x-iOSC) have similar two-stage degradation, a fast decay followed by slow degradation behavior, while PFN-iOSC shows more rapid PCE deterioration. The degradation mechanism of the first fast decay regarding $T1$ is mainly caused by water and the second slow decay of $T2$ is related to oxygen ingress in the device, as was observed similarly in Yang *et al.* work[42] The smaller values of $T1$ for all devices than $T2$ indicate that water diffusion is being more detrimental to this degradation process. The time constant $T2$ of PFN-iOSC (1260 h) shows the lowest value among the studied ETLs, suggesting that PFN-iOSC suffers more by the presence of oxygen than the metal oxide ETL-based iOSCs. On the other hand, the highest time constant $T2$ (4000 h) is observed in ZnO-iOSC and the second highest $T2$ (2526 h) is observed in TiO_x-iOSC. This result suggests that the use of metal oxides, especially ZnO, as an ETL in nonencapsulated iOSCs may be favorable to obtain more stable device performance parameters. The calculated parameter r defined as $A1/A2$ follows a behavior $r < 1$ for all nonencapsulated devices, showing a reliable measurement under the same conditions: dark ambient environment exposure.

Fig. 3 presents the behaviour of series and shunt resistances over shelf lifetime. As shown in Fig. 3a, the R_S of nonencapsulated iOSCs with different ETLs increases after 526 h exposure to ambient conditions in which the decay behaviour of R_S is observed similarly with the PCE decay behavior in Fig. 2a. R_S values keep constant from its initial time and start to increase at 3 h (T_{95}), 70 h (T_{90}), and 115 h (T_{90}) for PFN-, TiO_x- and ZnO-iOSCs, respectively. Afterwards, R_S values rise abruptly for PFN-, increase gradually for TiO_x- and increase steadily for ZnO-iOSCs until 526 h. Interestingly, in Fig. 3b, it is shown that the R_{Sh} of ZnO-iOSC was stable for 526 h, while those of PFN- and TiO_x-iOSCs showed a rapid decrease for 26 h (T_{80}) and 70 h (T_{90}), respectively, following the PCE decay behaviour. The most stable and the lowest R_S combined with the highest R_{Sh} values belong to ZnO-iOSC which is coherent with FF and PCE decay behaviour (see Fig. 2 and Table S2†). As the increase of R_S and decrease of R_{Sh} are followed by the FF and PCE decay, it is reasonable to suppose that the stability of the studied iOSCs exposed to ambient conditions is related to interface degradation, as observed in similar work.[43,44] This is in good agreement with the AFM measurement of each ETL fresh and degraded film, as shown in Fig. S4.† The difference between the root-mean-square (RMS) roughness of fresh and degraded ZnO films is very small (ΔRMS = 0.01 nm) compared to the PFN film (ΔRMS = 1.31 nm), which indicates an effective interfacial area between the ZnO layer and the active layer. The smoother the ETL film, the smaller the ETL/active layer interfacial area and the fewer the interface traps, leading to suppressed undesired charge recombination and leakage current, which reduces the FF.[45,46] This can be attributed to the function of the ZnO layer as a scavenging layer to prevent the diffusion of oxygen and water molecule ingress to the active layer.[17] Moreover, a better quality ZnO film than the other ETLs can help to passivate the blend/ETL interface layer from the interface defect due to the chemisorption of oxygen as trap states causing the concentration of free electrons to decrease.[47,48] Nevertheless, it is important to note that due to the complexity of the degradation mechanisms of each layer within the device, the information extracted solely from the J–V characteristics does not provide conclusive evidence to understand the dominating mechanism of performance deterioration. Therefore, a combined technique of time and frequency domains to perform shelf-lifetime degradation analysis is discussed more in detail in the following section.

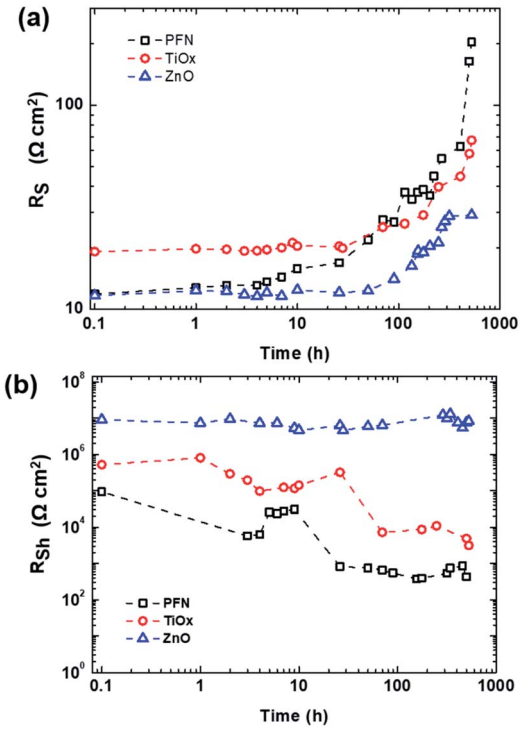

Fig. 3 (a) Series and (b) shunt resistances of the inverted PTB7-Th:$PC_{70}BM$-based device over shelf lifetime with different ETLs (PFN, TiO_x and ZnO) extracted from dark J–V measurements.

Transient photovoltage (TPV)/photocurrent (TPC) analysis

To investigate the effect of different ETLs on charge kinetics and recombination, fresh and degraded nonencapsulated iOSCs were measured under operando conditions by using charge extraction (CE) and transient photovoltage (TPV)/photocurrent (TPC) techniques. These techniques have been frequently employed to analyze the carrier losses and the carrier recombination in dye-sensitized solar cells and OSCs,[49–51] and more recently in perovskite solar cells.[52–54] Understanding the carrier loss mechanisms is key to increase solar cell efficiency. Therefore, we consider analyzing fresh and degraded devices as an important way to elucidate the different mechanisms at the device interfaces. While a brief description of the experimental procedure can be found in the Device characterization section, the technique is described in detail elsewhere.[55]

In general, the CE technique allows the measurement of accumulated charges and the TPV enables the study of carrier recombination decay under different light biases (solar cell

Open Access Article. Published on 15 November 2021. Downloaded on 2/12/2026 8:14:27 AM.
This article is licensed under a Creative Commons Attribution-NonCommercial 3.0 Unported Licence.

voltage as a result of light irradiation). In most kinds of solar cells, such as full-organic or dye-sensitized solar cells, photo-generated carriers are extracted before they recombine. In other words, the CE decay is always much faster than the TPV at the same light bias, as we can observe from our devices (see Fig. S5†). Nevertheless, the combination of TPV/TPC allows obtaining the differential capacitance (DC) as an alternative technique to CE.[56] Here we used both CE and DC techniques to accurately analyse the charge density of the devices (see an example in Fig. S6†).

For a comparison between iOSCs with different ETLs, we made sure that the film thicknesses are equal in all devices within the measurement error, *i.e.* ETL thicknesses close to 20 nm. Fig. 4a shows photo-generated charges stored in the fresh and degraded cells at equilibrium at different V_{OC} values, achieved by tuning the background illumination from the dark to 1 Sun equivalent. At first sight, the degraded samples showed higher charge density values for a given V_{OC}. In agreement with similar work recently reported,[32] this can be attributed to chemical reactions as a result of interlayer degradation originating near the interface. Meanwhile, the charge density for the fresh devices is very similar for the different ETLs and consistent with the observed V_{OC} (~0.8 V), and the increase in charge density upon degradation is different for each ETL and so less consistent with the V_{OC}. Charge density usually exhibited a linear and exponential part, attributed to the charges accumulated at the interfaces – known as geometrical capacitance – and within the bulk – chemical capacitance–, as depicted in Fig. S7.† By analyzing both separately, we obtained more information about how the degradation process affects the charge extraction of the devices depending on the ETL used. Fig. S7b† shows that TiO_x in degraded cells presents slightly higher charge density.

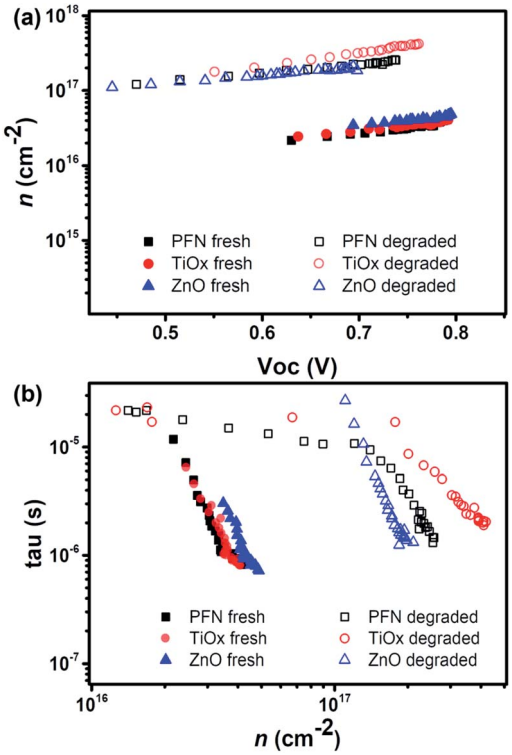

Fig. 4 (a) The charge density *vs.* V_{OC} and (b) the charge lifetime *vs.* charge density for fresh and degraded devices.

A change in recombination kinetics can be observed by looking at the charge density dependence of the carrier lifetime. Therefore, the carrier lifetimes (τ) obtained from the TPV decays of fresh and degraded devices are plotted as a function of charge density in Fig. 4b. There is an improvement in the carrier lifetime in the degraded devices, approximately 3 times longer than the fresh devices at a charge density of 2.5×10^{16} cm^{-2}.

These results are consistent with the increase in trap formation upon degradation (mainly due to oxygen and water penetration) as carrier lifetimes are shown to increase for given carrier densities. Due to the presence of traps, charges may spend a certain amount of time in these traps, before being released and so being recombined. We have seen that the increased carrier lifetime does not causes higher V_{OC} values for those degraded devices because to reach the same Fermi-level splitting, much higher charge density would now be needed compared to the fresh devices. We can also notice that, in general, lifetimes are similar for all devices, especially close to 1 Sun intensity, which indicates that the ETL properties do not have a significant influence on recombination kinetics.

Therefore, we can conclude from this section that, as we have not observed significant changes in recombination behavior and in the device ideality factor from light intensity dependency measurement (see Fig. S8†), the observed performance degradation is improbable to come from energy level changes. In this case, we can confirm that the degradation does not induce significant increases in trap-assisted recombination which may be one potential source of performance loss.

Impedance spectroscopy analysis

To obtain a deeper understanding of the degradation mechanism associated with the interfaces, we performed IS measurements on the same devices investigated by TPV/TPC. IS measures the phase shift and the amplitude of the current response obtained upon applying an AC voltage to the device at a given frequency. The frequency dependent measurements aid to explain the several mechanisms occurring at several interfaces.[57] Thus, the interface state will be distinguished more easily by IS than by TPV, in which all charges are forced to recombine.

The first approach to fit the experimental IS data of all fresh samples is to use an equivalent circuit model comprising one series resistance connected in series with three resistor/capacitor components (3RC). The 3RC equivalent circuit model can be employed to get information about each layer within the devices.[58,59] To properly fit the impedance data at higher frequencies (HFs), *i.e.* $f > 0.1$ MHz, for all fresh samples, the main effect to overcome is the reduction of the phase values. From the circuital point of view, a reduction of the $-Z''$ experimental value on the negative x-axis can only be explained by the presence of series inductance (L). The physical origin of the L

Open Access Article. Published on 15 November 2021. Downloaded on 2/12/2026 8:14:27 AM.
This article is licensed under a Creative Commons Attribution-NonCommercial 3.0 Unported Licence.

term could be related to wiring, although compensation was done before the measurement. An alternative origin could be the typical equivalent circuit of a capacitor at HF. A series resistance element (R_S) takes into consideration the ITO sheet resistance and three RC elements correspond to the capacitance and resistance of the ETL, the bulk active layer, and the hole transport layer (HTL). The geometrical capacitance (C_{geo}) values of each layer are listed in Table S3.† These values depend on the dielectric permittivity and the thickness of the layer, as expressed by eqn (S1).† The comparison of the different C_{geo} values of each layer and the fitting values enables us to predict the correlation between RC components.

The typical arc behavior with a single semi-circle is observed in the Cole–Cole plots (Fig. 5a) with one peak in the phase angle of Bode plots (Fig. 5b), suggesting the presence of RC components. Table S4† summarizes the extracted capacitance and resistance values from fitting the impedance spectra of all devices using the 3RC equivalent circuit model under open-circuit conditions. It is noticed that ITO sheet resistances depend on the ETL used, where a R_S value in the range of 10 Ω was expected. Among the fresh samples, at a given frequency, PFN-iOSCs demonstrate the lowest impedance value in the flat region of $|Z|$ *vs.* f compared to the metal oxide-ETL counterparts. These results corroborate the highest device performance obtained using PFN-ETL as the fresh device. It is worth noting that the fitted equivalent capacitance values (C_{fit}) of the bulk are higher than the C_{geo} of the blend by ≈3 nF. From the circuital point of view, an increase of C_{fit} compared to C_{geo} can only be explained by the presence of a parallel capacitance. Fig. S9† shows the equivalent circuit model used to fit the impedance spectra, allowing the interfacial density of states (D_{it}) of the blend and the traps created during the degradation process to be observed. This estimation is based on polymer metal–insulator–semiconductor (MIS) capacitor work.[60,61] The interface states are represented by an interface trap capacitance (C_{it}) in parallel with the capacitance of the semiconductor. C_{it} can be obtained by subtracting C_{geo} from C_{fit} ($C_{it} = C_{fit} - C_{geo}$), so the interface density of states $D_{it} = C_{it}/qA$ can be calculated as 4–6 × 10^{11} cm^{-2} eV^{-1} for PTB7-Th under open-circuit conditions, see Table 3. These values are within the range of values obtained for the interface density of states in P3HT.[62,63]

After degradation, as shown in Fig. 5c, a single semicircle behavior is still observed with the increased average diameter of the arcs over storage time for PFN-iOSCs under open-circuit conditions. A similar trend is observed for the other studied ETLs. The time degradation impedance characteristics have been examined by fitting these with an equivalent circuit model. Another common characteristic for PFN-, TiO_x- and ZnO-iOSCs is that the diameter of arcs decreases with increasing applied bias voltage, which can be related to the efficient charge

Table 3 Interface trap density (D_{it}) of all devices before and after degradation under open-circuit conditions

	$C_{it} = C_{fit} - C_{geo}$ (nF)		$D_{it} = C_{it}/QA$ (cm^{-2} eV^{-1})		
ETL	Fresh	Degraded	Fresh	Degraded	ΔD_{it} (%)
PFN	7	11	4.86×10^{11}	7.64×10^{11}	57
TiO_x	6	9	4.17×10^{11}	6.25×10^{11}	50
ZnO	9	10	6.25×10^{11}	6.94×10^{11}	11

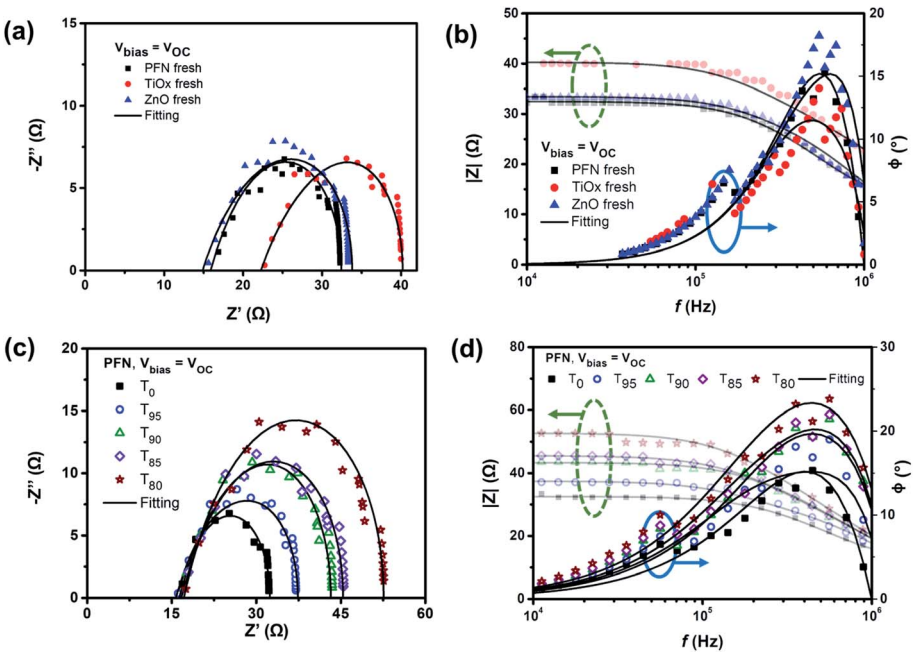

Fig. 5 (a) and (c) Cole–Cole plot and (b) and (d) Bode plot (modulus green-dashed arrow and phase blue-solid arrow) for (a) and (b) fresh devices using three different ETLs and (c) and (d) degraded PFN-based non-encapsulated devices over degradation time (T_0, T_{95}, T_{90}, T_{85}, and T_{80}) measured under open-circuit conditions. The experimental results were fitted using a RC circuit model (solid lines) shown in Fig. S9.†

Open Access Article. Published on 15 November 2021. Downloaded on 2/12/2026 8:14:27 AM.
This article is licensed under a Creative Commons Attribution-NonCommercial 3.0 Unported Licence.

extraction.[58] Fig. 5d exhibits the $|Z|$–f relation of PFN-iOSC over degradation time in which the impedance values increase as the degradation time increases and the difference is more prominent in the lower frequencies (LF) region, suggesting that the LF feature becomes evident in the degraded cells. As compared to C_{geo} values, the fitted capacitance values of charge transport layers (ETL and HTL) appear to be the same and remain constant during degradation, see Table S4.† However, the fitted capacitance values of the blend in all samples are higher than those of geometrical values and their values increase with the degradation time. As shown in Table 3, the interface density of states values after a degradation time of 526 hours increases by 57%, 50% and 11% for PFN-, TiO_x- and ZnO-iOSCs, respectively, in good agreement with the increase of the dark leakage current–voltage characteristic in the degraded devices. The highest degradation of the PFN iOSC correlates with the largest increase of the interface density of states values for this sample. Thus, we can assume that the traps created by water and oxygen will modify only the bulk interface with the ETL and HTL, whereas the ETL and HTL are fully depleted layers.

Combined steady-state and transient techniques

To obtain an excellent agreement within the steady-state and transient techniques, we compare both the ideality factors obtained from dark J–V modelling results with TPV/TPC studies. As shown in Fig. 6, the charge carrier density and charge carrier lifetime both exponentially depend on V_{OC}, following eqn (2) and (3):

$$n = n_0 \times \exp\left(\frac{qV_{OC}}{n_n kT}\right) \tag{2}$$

$$\tau_{\Delta n} = \tau_{\Delta n_0} \times \exp\left(\frac{qV_{OC}}{n_\tau kT}\right) \tag{3}$$

where n_n and n_τ defined as the ideality factors correspond to the carrier density and carrier lifetime, respectively.[64] In previous work, the slopes in the semilogarithmic plots of Fig. 6 were described by the parameters $\gamma = q/n_n kT$ and $\beta = q/n_\tau kT$.[65] All the n_n and n_τ ideality factors obtained from Fig. 6a are summarized in Table 4. It is important to notice that fresh devices, but not after degradation, show an exponential fitting with two different regions. One region at higher voltages (0.75–0.79 V), which can be attributed to bulk dynamics, and another region (0.63–0.75 V) attributed to the capacitive contribution.

Charge extraction and transient photovoltage techniques can be used to determine not only charge carrier densities and carrier recombination but also steady-state parameters like the ideality factor n_{id}. The diode ideality factor is correlated with n_n (at higher V_{OC} voltages, *i.e.* 0.75–0.79 V) and n_τ by following eqn (4):

$$n_{id}^{-1} = n_n^{-1} + n_\tau^{-1} \tag{4}$$

Although the ideality factors were determined in two different ways – from J–V characteristics and from CE and TPV techniques – both n_{id} found to be identical for our solar cells. These n_{id} values have already been compared by other authors,[64,66,67] where they obtained identical ideality factors as in our case, very close values or slightly underestimated compared to the steady-state values. Therefore, the good agreement of steady-state and transient techniques demonstrates the validity of the Shockley model for this kind of solar cell.

To validate the aforementioned assumption and the proposed model of D_{it}, we checked the time constant obtained from the IS and TPV measurements. The similar carrier lifetime values between the two techniques should correlate with each other when the recombination took place. The characteristic time constant from the RC circuit of IS data under open-circuit conditions is given by $\tau = R \times C$. The time constants measured from both techniques for PFN-iOSCs are shown in Fig. 7. On one side, each V_{OC} bias point from IS data corresponds to a different degradation time with the same illumination, whereas on the other side those of TPV data correspond to the same

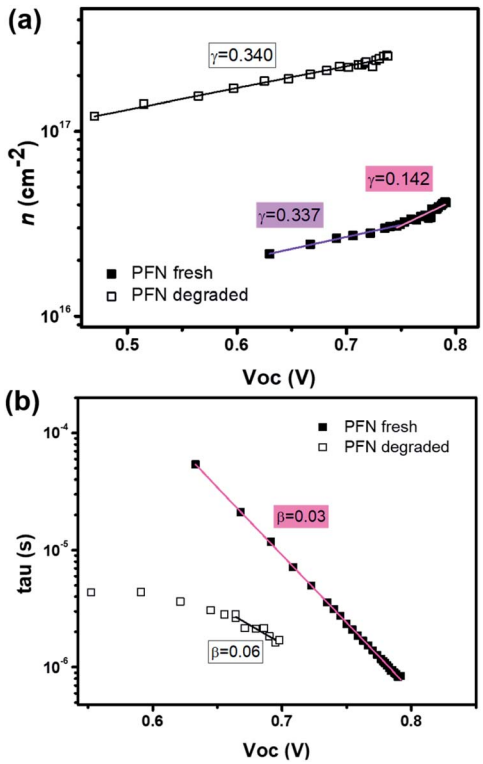

Fig. 6 The fitted data of (a) charge carrier density and (b) charge carrier lifetime *versus* open circuit voltage from CE and TPV measurements using eqn (2) and (3) for the fresh and degraded PFN-iOSCs.

Table 4 Summary of ideality factors determined by transient (CE and TPV) techniques and J–V characteristics

	n_n	n_τ	n_{id} (CEn_n/TPVn_τ)	n_{id} (J–V)
PFN fresh	5.48 (V_{OC} > 0.75)	1.42	1.12	1.11
	13.01 (V_{OC} < 0.75)	—	—	
PFN deg.	13.13	2.31	1.96	1.91

Open Access Article. Published on 15 November 2021. Downloaded on 2/12/2026 8:14:27 AM.
This article is licensed under a Creative Commons Attribution-NonCommercial 3.0 Unported Licence.

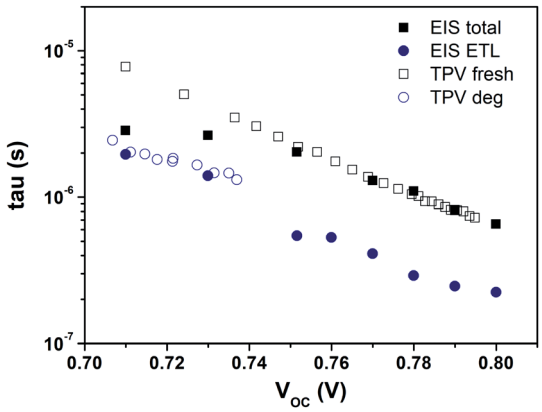

Fig. 7 IS time constant under open-circuit conditions compared to the carrier lifetimes extracted from TPV measurements for the fresh and degraded PFN-iOSCs.

degradation time with different illumination. A good agreement is observed between the total τ of IS in the V_{OC} range from 0.8 V (fresh sample) to 0.74 V (degraded sample 176 h) and the total τ of TPV fresh PFN-iOSCs data from 0.8 V (the highest light intensity) to 0.74 V (lower light intensity). The time constant obtained from IS in the V_{OC} range from 0.74 V to 0.70 V (degraded 526 h) mismatched the pattern of TPV fresh and follow the pattern of TPV degraded data. To determine which layer is the primary cause of shelf degradation, we analyze the contribution of each layer. We found that by fitting the ETL time constant, $\tau_{ETL} = R_{ETL} \times C_{ETL}$, it follows the trend of τ extracted from TPV for degraded devices at 267 h and 526 h. The relative τ contribution of each layer to the total τ is shown in Fig. S10.† In fresh devices, almost 30% contribution of τ values is due to the HTL, whereas in the degraded devices, almost 70% contribution of τ values is due to the ETL. This result is in good agreement with the generation of interfacial traps in the degradation process. It suggests that the interfacial defects, demonstrated by the presence of the interface state effect, D_{it}, can be the main cause of degradation.

Conclusions

In summary, we performed both frequency and time-domain characterization techniques to investigate the shelf-life degradation of ITO/ETL/PTB7-Th:$PC_{70}BM$/V_2O_5/Ag using three different ETLs, one organic-based ETL (PFN) and two metal oxide-based ETLs (TiO_x and ZnO), following the ISOS-D1 protocol. Both techniques can provide real information on how different ETLs were degraded, affecting the stability of the active layer over storage time. We have found that the main cause of degradation is the formation of interface traps in the r dark and upon air exposure. TPV measurements give an insight into the interfacial recombination processes, and particularly they show an increase of trap density in the active layer due to the degradation. From the IS data, it is possible not only to determine the relative contribution of each layer to the total time constant but also to estimate the increase of the interface density of states values due to the degradation process. Modelling dark current–voltage (*J*–*V*) characteristic and atomic force microscopy (AFM) measurements further confirm the presence of traps in the degraded devices.

Conflicts of interest

The authors declare that there is no conflict of interest.

Acknowledgements

A. A. A. T. acknowledges the financial support from the European Union's Horizon 2020 research and innovation programme under the Marie Skłodowska-Curie grant agreement No. 713679. This work was further supported by the Spanish Ministerio de Ciencia, Innovación y Universidades (MICINN/FEDER) RTI2018-094040-B-I00, by the Agency for Management of University and Research Grants (AGAUR) ref. 2017-SGR-1527, by Diputació de Tarragona 2021CM14 and from the Catalan Institution for Research and Advanced Studies (ICREA) under the ICREA Academia Award. ICIQ and ICREA are also acknowledge for its contribution with the transient photo-induced measurements and discussion of the results.

References

1 B. Zhao, Z. He, X. Cheng, D. Qin, M. Yun, M. Wang, X. Huang, J. Wu, H. Wu and Y. Cao, *J. Mater. Chem. C*, 2014, **2**, 5077–5082.
2 A. Gusain, R. M. Faria and P. B. Miranda, *Front. Chem.*, 2019, **7**, 1–25.
3 V. I. Madogni, B. Kounouhéwa, A. Akpo, M. Agbomahéna, S. A. Hounkpatin and C. N. Awanou, *Chem. Phys. Lett.*, 2015, **640**, 201–214.
4 Z. Hu, J. Wang, X. Ma, J. Gao, C. Xu, X. Wang, X. Zhang, Z. Wang and F. Zhang, *J. Mater. Chem. A*, 2021, **9**, 6797–6804.
5 Y. Wang, F. Wang, J. Gao, Y. Yan, X. Wang, X. Wang, C. Xu, X. Ma, J. Zhang and F. Zhang, *J. Mater. Chem. C*, 2021, **9**, 9892–9898.
6 Y. Lin, B. Adilbekova, Y. Firdaus, E. Yengel, H. Faber, M. Sajjad, X. Zheng, E. Yarali, A. Seitkhan, O. M. Bakr, A. El-Labban, U. Schwingenschlögl, V. Tung, I. McCulloch, F. Laquai and T. D. Anthopoulos, *Adv. Mater.*, 2019, **1902965**, 1902965.
7 Y. Lin, Y. Firdaus, M. I. Nugraha, F. Liu, S. Karuthedath, A. Emwas, W. Zhang, A. Seitkhan, M. Neophytou, H. Faber, E. Yengel, I. Mcculloch, L. Tsetseris, F. Laquai and T. D. Anthopoulos, *Adv. Sci.*, 2020, **1903419**, 1–9.
8 Q. Liu, Y. Jiang, K. Jin, J. Qin, J. Xu, W. Li, J. Xiong and J. Liu, *Sci. Bull.*, 2020, **65**, 272–275.
9 W. R. Mateker and M. D. McGehee, *Adv. Mater.*, 2017, **1603940**, 1–16.
10 X. Xu, J. Xiao, G. Zhang, L. Wei, X. Jiao, H. L. Yip and Y. Cao, *Sci. Bull.*, 2020, **65**, 208–216.
11 M. J. Newman, E. M. Speller, J. Barbé, J. Luke, M. Li, Z. Wang, S. M. Jain, J. Kim, H. Ka, H. Lee, M. J. Newman, E. M. Speller, J. Barbé, J. Luke, M. Li, Z. Wang, S. M. Jain, J. Kim, H. Ka,

Open Access Article. Published on 15 November 2021. Downloaded on 2/12/2026 8:14:27 AM.
This article is licensed under a Creative Commons Attribution-NonCommercial 3.0 Unported Licence.

H. Lee and W. C. Tsoi, *Sci. Technol. Adv. Mater.*, 2018, **6996**, 1–9.
12 A. A. A. Torimtubun, J. Follana-Berná, J. G. Sánchez, J. Pallarès, Á. Sastre-Santos and L. F. Marsal, *ACS Appl. Energy Mater.*, 2021, **4**, 5201–5211.
13 P. Cheng and X. Zhan, *Chem. Soc. Rev.*, 2016, **45**, 2544–2582.
14 L. Duan and A. Uddin, *Adv. Sci.*, 2020, **1903259**, 1–39.
15 Q. An, F. Zhang, W. Gao, Q. Sun, M. Zhang, C. Yang and J. Zhang, *Nano Energy*, 2018, **45**, 177–183.
16 B. Ecker, J. C. Nolasco, J. Pallarés, L. F. Marsal, J. Posdorfer, J. Parisi and E. Von Hauff, *Adv. Funct. Mater.*, 2011, **21**, 2705–2711.
17 J. G. Sánchez, V. S. Balderrama, M. Estrada, E. Osorio, J. Ferré-Borrull, L. F. Marsal and J. Pallarès, *Sol. Energy*, 2017, **150**, 147–155.
18 V. S. Balderrama, M. Estrada, P. L. Han, P. Granero, J. Pallarés, J. Ferré-Borrull and L. F. Marsal, *Sol. Energy Mater. Sol. Cells*, 2014, **125**, 155–163.
19 I. I. Jeon and Y. Matsuo, *Sol. Energy Mater. Sol. Cells*, 2015, **140**, 335–343.
20 Y. Wang, H. Cong, B. Yu, Z. Zhang and X. Zhan, *Materials*, 2017, **10**, 1064.
21 A. A. A. Torimtubun, J. G. Sanchez, J. Pallares and L. F. Marsal, in *2020 IEEE Latin America Electron Devices Conference (LAEDC)*, IEEE, San Jose, Costa Rica, 2020, pp. 1–4.
22 D. Yang, P. Fu, F. Zhang, N. Wang, J. Zhang and C. Li, *J. Mater. Chem. A*, 2014, **2**, 17281–17285.
23 M. Prosa, M. Tessarolo, M. Bolognesi, O. Margeat, D. Gedefaw, M. Gaceur, C. Videlot-Ackermann, M. R. Andersson, M. Muccini, M. Seri and J. Ackermann, *ACS Appl. Mater. Interfaces*, 2016, **8**, 1635–1643.
24 F. X. Xie, W. C. H. Choy, W. E. I. Sha, D. Zhang, S. Zhang, X. Li, C. W. Leung and J. Hou, *Energy Environ. Sci.*, 2013, **6**, 3372–3379.
25 A. A. A. Torimtubun, J. G. Sánchez, J. Pallarès and L. F. Marsal, *Sustainable Energy Fuels*, 2020, **4**, 3378–3387.
26 A. Sacco, *Renewable Sustainable Energy Rev.*, 2017, **79**, 814–829.
27 W. Yan, M. M. Huo, R. Hu and Y. Wang, *RSC Adv.*, 2019, **9**, 1734–1740.
28 M. Jiang, H. R. Bai, H. F. Zhi, J. K. Sun, J. L. Wang, F. Zhang and Q. An, *ACS Energy Lett.*, 2021, **6**, 2898–2906.
29 M. Jiang, H. Bai, H. Zhi, L. Yan, H. Y. Woo, L. Tong, J. Wang, F. Zhang and Q. An, *Energy Environ. Sci.*, 2021, **14**, 3945–3953.
30 J. Jiménez-López and E. Palomares, *Nanoscale*, 2019, **11**, 20024–20029.
31 E. Von Hauff, *J. Phys. Chem. C*, 2019, **123**, 11329–11346.
32 A. Pockett, H. K. H. Lee, B. L. Coles, W. C. Tsoi and M. J. Carnie, *Nanoscale*, 2019, **11**, 10872–10883.
33 M. O. Reese, S. A. Gevorgyan, M. Jørgensen, E. Bundgaard, S. R. Kurtz, D. S. Ginley, D. C. Olson, M. T. Lloyd, P. Morvillo, E. A. Katz, A. Elschner, O. Haillant, T. R. Currier, V. Shrotriya, M. Hermenau, M. Riede, K. R. Kirov, G. Trimmel, T. Rath, O. Inganäs, F. Zhang, M. Andersson, K. Tvingstedt, M. Lira-Cantu, D. Laird, C. McGuiness, S. Gowrisanker, M. Pannone, M. Xiao, J. Hauch, R. Steim, D. M. Delongchamp, R. Rösch, H. Hoppe, N. Espinosa, A. Urbina, G. Yaman-Uzunoglu, J. B. Bonekamp, A. J. J. M. Van Breemen, C. Girotto, E. Voroshazi and F. C. Krebs, *Sol. Energy Mater. Sol. Cells*, 2011, **95**, 1253–1267.
34 N. Chaturvedi, S. Kumar Swami, A. Kumar and V. Dutta, *Sol. Energy Mater. Sol. Cells*, 2014, **126**, 74–82.
35 J. Pallarès, R. Cabré, L. F. Marsal and R. E. I. Schropp, *J. Appl. Phys.*, 2006, **100**, 2–7.
36 N. Grossiord, J. M. Kroon, R. Andriessen and P. W. M. Blom, *Org. Electron.*, 2012, **13**, 432–456.
37 A. Guerrero, N. F. Montcada, J. Ajuria, I. Etxebarria, R. Pacios, G. Garcia-Belmonte and E. Palomares, *J. Mater. Chem. A*, 2013, **1**, 12345–12354.
38 M. A. Islam, M. Hasanuzzaman and N. A. Rahim, *IEEE Journal of Photovoltaics*, 2018, **8**, 1259–1265.
39 K. Kawano, R. Pacios, D. Poplavskyy, J. Nelson, D. D. C. Bradley and J. R. Durrant, *Sol. Energy Mater. Sol. Cells*, 2006, **90**, 3520–3530.
40 A. Sacramento, V. S. Balderrama, M. Ramírez-como, L. F. Marsal and M. Estrada, *Sol. Energy*, 2020, **198**, 419–426.
41 J. Kong, S. Song, M. Yoo, G. Y. Lee, O. Kwon, J. K. Park, H. Back, G. Kim, S. H. Lee, H. Suh and K. Lee, *Nat. Commun.*, 2014, **5**, 1–8.
42 H. Bin Yang, Q. L. Song, C. Gong and C. M. Li, *Sol. Energy Mater. Sol. Cells*, 2010, **94**, 846–849.
43 K. Norrman, M. V. Madsen, S. A. Gevorgyan and F. C. Krebs, *J. Am. Chem. Soc.*, 2010, **132**, 16883–16892.
44 A. Guerrero, M. Pfannmöller, A. Kovalenko, T. S. Ripolles, H. Heidari, S. Bals, L. D. Kaufmann, J. Bisquert and G. Garcia-Belmonte, *Org. Electron.*, 2015, **16**, 227–233.
45 Z. Ma, Z. Tang, E. Wang, M. R. Andersson, O. Inganäs and F. Zhang, *J. Phys. Chem. C*, 2012, **116**, 24462–24468.
46 B. Qi and J. Wang, *Phys. Chem. Chem. Phys.*, 2013, **15**, 8972–8982.
47 M. R. Lilliedal, A. J. Medford, M. V. Madsen, K. Norrman and F. C. Krebs, *Sol. Energy Mater. Sol. Cells*, 2010, **94**, 2018–2031.
48 M. Ramírez-Como, A. Sacramento, J. G. Sánchez, M. Estrada, J. Pallarès, V. S. Balderrama and L. F. Marsal, *Sol. Energy Mater. Sol. Cells*, 2021, **230**, 111265.
49 L. Xu, C. Aumaitre, Y. Kervella, G. Lapertot, C. Rodríguez-seco, E. Palomares, R. Demadrille and P. Reiss, *Adv. Funct. Mater.*, 2018, 1706291.
50 V. S. Balderrama, J. G. Sánchez, G. Lastra, W. Cambarau, S. Arias, J. Pallarès, E. Palomares, M. Estrada and L. F. Marsal, *J. Mater. Chem. A*, 2018, **6**, 22534–22544.
51 S. M. Tuladhar, M. Azzouzi, F. Delval, J. Yao, A. A. Y. Guilbert, T. Kirchartz, N. F. Montcada, R. Dominguez, F. Langa, E. Palomares and J. Nelson, *ACS Energy Lett.*, 2016, **1**, 302–308.
52 C. Rodríguez-Seco, M. Méndez, C. Roldán-Carmona, R. Pudi, M. K. Nazeeruddin and E. J. Palomares, *Angew. Chem., Int. Ed.*, 2020, 1–6.
53 N. Y. Nia, M. Méndez, A. Di Carlo and E. Palomares, *Philos. Trans. R. Soc., A*, 2019, **377**, 1–8.

Open Access Article. Published on 15 November 2021. Downloaded on 2/12/2026 8:14:27 AM.
This article is licensed under a Creative Commons Attribution-NonCommercial 3.0 Unported Licence.

54 N. F. Montcada, M. Méndez, K. T. Cho, M. K. Nazeeruddin and E. Palomares, *Nanoscale*, 2018, **10**, 6155–6158.
55 E. Palomares, N. F. Montcada, M. Méndez, J. Jiménez-López, W. Yang and G. Boschloo, in *Characterization Techniques for Perovskite Solar Cell Materials*, 2019, pp. 161–180.
56 A. Maurano, C. G. Shuttle, R. Hamilton, A. M. Ballantyne, J. Nelson, W. Zhang, M. Heeney and J. R. Durrant, *J. Phys. Chem. C*, 2011, **115**, 5947–5957.
57 S. K. Gupta, L. S. Pali and A. Garg, *Sol. Energy*, 2019, **178**, 133–141.
58 E. Osorio, J. G. Sánchez, L. N. Acquaroli, M. Pacio, J. Ferré-Borrull, J. Pallarès and L. F. Marsal, *ACS Omega*, 2017, **2**, 3091–3097.
59 A. A. A. Torimtubun, J. G. Sanchez, J. Pallares and L. F. Marsal, *IEEE J. Electron Devices Soc.*, 2021, **9**, 484–491.
60 I. Torres and D. M. Taylor, *J. Appl. Phys.*, 2005, **98**, 073710.
61 H. Hirwa, S. Pittner and V. Wagner, *Org. Electron.*, 2015, **24**, 303–314.
62 C. M. Proctor, C. Kim, D. Neher and T. Q. Nguyen, *Adv. Funct. Mater.*, 2013, **23**, 3584–3594.
63 A. Foertig, J. Kniepert, M. Gluecker, T. Brenner, V. Dyakonov, D. Neher and C. Deibel, *Adv. Funct. Mater.*, 2014, **24**, 1306–1311.
64 A. Foertig, J. Rauh, V. Dyakonov and C. Deibel, *Phys. Rev. B: Condens. Matter Mater. Phys.*, 2012, **86**, 1–7.
65 C. G. Shuttle, B. O'Regan, A. M. Ballantyne, J. Nelson, D. D. C. Bradley, J. De Mello and J. R. Durrant, *Appl. Phys. Lett.*, 2008, **92**, 1–4.
66 D. Kiermasch, L. Gil-Escrig, A. Baumann, H. J. Bolink, V. Dyakonov and K. Tvingstedt, *J. Mater. Chem. A*, 2019, **7**, 14712–14722.
67 T. Kirchartz, B. E. Pieters, J. Kirkpatrick, U. Rau and J. Nelson, *Phys. Rev. B: Condens. Matter Mater. Phys.*, 2011, **83**, 1–13.

 This journal is © The Royal Society of Chemistry 2021